# Unsaturated flow quasi-three-dimensional fractured medium with spatially variable aperture

2 **AUTHORS**, INCLUDING:

Constantinos V. Chrysikopoulos
Technical University of Crete

**143** PUBLICATIONS **1,991** CITATIONS

# Unsaturated flow in a quasi-three-dimensional fractured medium with spatially variable aperture

Assem Abdel-Salam and Constantinos V. Chrysikopoulos

Department of Civil and Environmental Engineering, University of California, Irvine

**Abstract.** Transient moisture flow in a variably saturated quasi-three-dimensional fracture-rock matrix system is investigated. The fracture is assumed to possess a spatially variable aperture in its two-dimensional plane, whereas the rock matrix is treated as a two-dimensional homogeneous and tight porous medium. The aperture fluctuations in the fracture plane are described stochastically. Moisture exchange between the fracture and the rock matrix is accounted for via an advective coupling term that governs the transfer of moisture at the fracture-matrix interface and takes into account the effect of a fracture-surface coating material. Although the variable aperture fracture is two-dimensional, the coupling term between the fracture and the rock matrix accounts for the three-dimensional nature of the physical system. The stochastic nonlinear set of partial differential equations is solved numerically by the Galerkin finite element method in conjunction with the Picard iterative scheme and an automatic time step marching. Simulations are performed to investigate phenomena which have been ignored in previous studies. It is demonstrated that, for the case of no moisture exchange with the rock matrix, the moisture follows preferential flow paths within the fracture plane and exhibits pronounced fingering effects. Furthermore, it is shown that the larger the fracture aperture fluctuations the more extended the moisture flow in the fracture. In addition, for the case where there exists moisture exchange with the rock matrix, the movement of the moisture front is considerably reduced, whereas fracture-surface coatings tend to slow down moisture absorption by the rock matrix.

## Introduction

Unsaturated fluid flow in fractured media is recently receiving substantial attention, because terminal waste storage in fractured media can possibly threaten the integrity of deeper aquifers in case of accidental leaks [e.g., *Evans and Nicholson*, 1987; *Pruess and Wang*, 1987; *Pruess and Tsang*, 1990; *Martinez et al.*, 1992; *Kwicklis and Healy*, 1993]. An example is the Yucca Mountain area in southwestern Nevada, which is being evaluated as a potential site for the first high-level nuclear waste repository in the United States [*U.S. Department of Energy* 1986]. In case of leaks the anticipated behavior of disposed wastes is dependent upon the characteristics of the medium, which govern fluid flow, fluid interactions with the rock matrix, and consequently, contaminant transport. Obviously, the problem is not trivial, and recent studies focused on unsaturated flow in fractured media overlook one or more significant aspects (e.g., fluid interaction with the rock matrix adjacent to the fracture and fracture aperture variability).

In saturated fractured rocks, flow occurs primarily through fractures, and fluid movement within the rock matrix surrounding fractures is negligible compared to that in fractures. This is because the saturated hydraulic conductivity of the rock matrix is several orders of magnitude smaller than the saturated hydraulic conductivity of fractures [*Pruess and Wang*, 1987]. However, unsaturated hydraulic conductivity is highly dependent upon the moisture content present in the system [*Evans and Nicholson*, 1987]. As the pressure head potential decreases

from zero at saturation to progressively negative values during desaturation, areas in the fracture with larger apertures drain first and cause a decrease in the hydraulic conductivity of the fracture. The hydraulic conductivity of the rock matrix also decreases with decreasing pressure head potential but at a smaller rate compared to that of the fracture. This is because the pore sizes in the rock matrix are much smaller than the fracture apertures. Therefore, at some point the flow in the rock matrix may be close or even exceed the flow in the fracture, and flow in the rock matrix cannot be neglected anymore.

Fluids present in fractures can be imbibed into the rock matrix by capillary suction forces at the fracture-matrix interface. The existence of a low permeability mineralized layer or coating at this interface may substantially reduce matrix imbibition and could consequently result in fracture-dominated flow [*Thoma et al.*, 1992]. Coating material typically found in the Yucca mountain region include manganese oxides, manganates, iron oxides, iron hydroxides, silica, zeolites, smectites, or carbonates [*Carlos*, 1985].

Several unsaturated flow models in fractured media have been presented in the literature. *Pruess and Tsang* [1990] modeled steady flow in a variable aperture fracture without moisture exchange with the rock matrix. The emphasis of their work was to develop characteristic relationships between unsaturated hydraulic conductivity, pressure head, and moisture content. *Kwicklis and Healy* [1993] extended *Pruess and Tsang*'s [1990] steady state flow model to a simple idealized discrete fracture network with impermeable rock matrix. Other researchers modeled unsaturated flow by replacing the matrix-fracture system with an equivalent porous medium [e.g., *Wilson and Dudley*, 1987; *Dykhuizen*, 1987]. *Nitao and Buscheck* [1991]
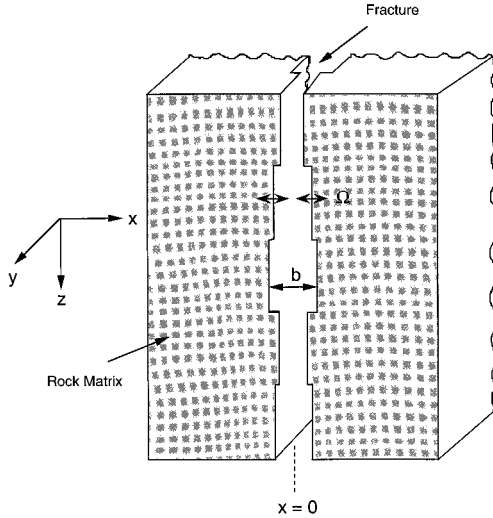
**Figure 1.** Schematic illustration of a vertical cross section in the fracture-rock matrix system with spatially variable aperture ($\Omega$ is the cross-flow coupling term between the fracture and the rock matrix and $b$ is the aperture).

modeled flow in a fracture idealized as two parallel plates with a coupling cross-flow term accounting for the exchange of fluids between the fracture and the rock matrix. *Gerke and van Genuchten* [1993] modeled one-dimensional unsteady vertical flow in a two-porosity system with a coupling cross-flow moisture exchange term.

In this study, a comprehensive mathematical model describing unsaturated moisture flow in a quasi-three-dimensional, fracture-rock matrix system with spatially variable aperture is presented. The pressure head potential field, for each realization of the aperture fluctuations, is determined by numerically solving a system of governing flow equations in the fracture and the rock matrix with a coupling term that accounts for fluid transfer at the fracture-matrix interface and the presence of a fracture-surface coating material. The Galerkin finite element method with two-dimensional triangular elements and linear basis functions is used to discretize the governing set of nonlinear partial differential equations. Several simulations are performed, in order to examine the behavior of the system studied under different physical conditions.

## Model Development

The physical system considered in this study is a quasi-three-dimensional spatially variable aperture fracture-rock matrix (see Figure 1). The assumption of a spatially variable aperture is consistent with observations from studies conducted in several field and laboratory experiments which show that the aperture in the fracture plane takes on a range of values [e.g., *Neretnieks*, 1985; *Abelin*, 1986; *Bourke*, 1987]. The hypothetical fracture used here is 8 m long and 4 m wide. The fracture aperture is assumed to be a stationary stochastic variable that follows a lognormal distribution with mean 1.65 $\mu$m (corresponding to approximately 45 $\mu$m on a linear scale) and standard deviation of the log of the apertures 0.43 $\mu$m and varies spatially according to an exponential autocovariance function with an isotropic spatial correlation scale 0.3 m [*Abdel-Salam and Chrysikopoulos*, 1995]. Random realizations of the aperture fluctuations for a fracture with equal-size grid spacing

(0.2 m in both the $y$ and $z$ directions) are generated using the geostatistical code COVAR [*Williams and El-Kadi*, 1986]. The grid used consists of 21 by 41 nodes in the $y$ and $z$ directions, respectively. Figure 2 shows a single realization of the aperture field in the fracture plane. Clearly, the fracture comprises a large variety of aperture sizes ranging from less than 9 $\mu$m (white) to 300 $\mu$m (black).

The transient unsaturated flow equation in a fracture with spatially variable aperture and moisture exchange with the rock matrix is derived from mass balance considerations over a representative fracture volume and is given as [*Abdel-Salam*, 1995]

$$b(y, z)C_f \frac{\partial \psi_f(t, y, z)}{\partial t}$$

$$= \frac{\gamma}{12\mu} \frac{\partial}{\partial z} \left[ b^3(y, z)k_{r_f} \left( \frac{\partial \psi_f(t, y, z)}{\partial z} - 1 \right) \right] + \frac{\gamma}{12\mu}$$

$$\cdot \frac{\partial}{\partial y} \left[ b^3(y, z)k_{r_f} \frac{\partial \psi_f(t, y, z)}{\partial y} \right] - \Omega(t, x, y, z), \qquad (1)$$

where $C(\psi) = d\theta/d\psi$ is the specific moisture capacity; $\psi$ is the pressure head potential; $b$ is the fracture aperture at location $(y, z)$; $k_r(\psi)$ is the relative permeability, which ranges between zero for entirely air flow and one for entirely water flow; $\Omega$ is the fracture-rock matrix cross-flow term; $\gamma$ is the fluid specific weight; $\mu$ is the fluid dynamic viscosity; $t$ is time; $y$ is a horizontal spatial coordinate along the fracture width; $z$ is a vertical spatial coordinate, which is measured positive downward; and the subscript $f$ refers to the fracture. For the derivation of the preceding equation, Darcy's law as applied to unsaturated fractures and the definition for the saturated hydraulic conductivity in a fracture segment formed by two parallel plates under incompressible laminar flow conditions ($K_f = \gamma b^2/12\mu$) have been employed. It should also be noted
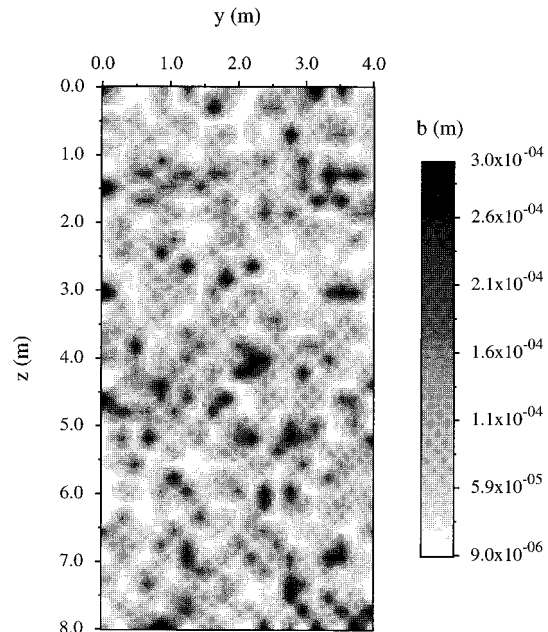


**Figure 2.** A single realization of the aperture spatial distribution in the fracture plane. The coded scale illustrates apertures between 9 and 300 $\mu$m (here $l_y = 4.0$ m and $l_z = 8.0$ m).

that (1) is a stochastic partial differential equation, because one of its parameters, namely $b$, is a stochastic variable.

The pressure head based partial differential equation describing transient unsaturated flow in a homogeneous isotropic rock matrix can be written as follows

$$C_m \frac{\partial \psi_m(t, x, y, z)}{\partial t} = K_m \frac{\partial}{\partial z}\left[k_{r_m}\left(\frac{\partial \psi_m(t, x, y, z)}{\partial z} - 1\right)\right]$$

$$+ K_m \frac{\partial}{\partial x}\left[k_{r_m} \frac{\partial \psi_m(t, x, y, z)}{\partial x}\right], \qquad (2)$$

where $K$ is the rock matrix saturated hydraulic conductivity, $x$ is a horizontal coordinate perpendicular to the fracture plane, and the subscript $m$ refers to the rock matrix. In the interest of computational simplicity, (2) is solved by not accounting for any moisture flow in the $y$ direction.

The derivation of the governing equations (1) and (2) is based on the assumptions that (1) fluid flow is accounted for only in the liquid phase, (2) adsorption of moisture onto fracture surfaces is negligible, and (3) air remains at constant atmospheric pressure at all times.

The initial and boundary conditions for the fracture-rock matrix system studied in this work are

$$\psi_f(0, y, z) = \psi_{if}, \qquad (3)$$

$$\psi_f(t, y, 0) = \psi_0, \qquad (4)$$

$$\partial \psi_f(t, y, l_z)/\partial z = 0, \qquad (5)$$

$$\partial \psi_f(t, 0, z)/\partial y = 0, \qquad (6)$$

$$\partial \psi_f(t, l_y, z)/\partial y = 0, \qquad (7)$$

$$\psi_m(0, x, y, z) = \psi_{i_m}, \qquad (8)$$

$$\psi_m(t, b/2, y, z) = \psi_f(t, y, z), \qquad (9)$$

$$\partial \psi_m(t, l_x, y, z)/\partial x = 0, \qquad (10)$$

$$\partial \psi_m(t, x, y, 0)/\partial z = 0, \qquad (11)$$

$$\partial \psi_m(t, x, y, l_z)/\partial z = 0, \qquad (12)$$

where $\psi_i$ is the initial pressure head potential; $\psi_0$ is the prescribed pressure head potential at the top boundary of the fracture; $l_z = 8$ m is the fracture-rock matrix length; $l_y = 4$ m is the width of the fracture; and $l_x$ is some representative depth into the rock matrix, which in this work is assumed to be 1 m. Equations (3) and (8) describe the initial conditions in the fracture and the rock matrix, respectively. Equation (4) implies that the fracture is subjected to a constant pressure head at the top boundary. Condition (9) implies an equilibrium in the pressure head potential at the fracture-rock matrix interface, which also indicates that there is negligible resistance to moisture flow between the fracture and the rock matrix. Equations (6), (7), (10), and (11) describe no-flow boundaries, whereas (5) and (12) imply free draining bottom boundary conditions in the fracture and rock matrix, respectively. Although the free draining boundary conditions (5) and (12) have the same mathematical form as the no-flux boundary conditions (6), (7), (10), and (11), nevertheless, their physical interpretation is different. This is because vertical flow in unsaturated zones is governed by capillary and gravitational forces, whereas horizontal flow is governed only by capillary forces. A no-flux boundary

condition equivalent to (5) would read $\partial \psi_f(t, y, l_z)/\partial z - 1 = 0$ [Kool and van Genuchten, 1991].

The cross-flow coupling term ($\Omega$) accounts for the transfer of fluid between the fracture and the rock matrix at the fracture-rock matrix interface. This term provides a means of including three-dimensional effects into the two-dimensional fracture model and is expressed as [Nitao and Buscheck, 1991]

$$\Omega(t, x, y, z) = -2K_e k_{r_m} \frac{\partial \psi_m}{\partial x}\bigg|_{x=b/2}, \qquad (13)$$

where $K_e$ is the fracture-surface effective hydraulic conductivity, which takes into account the effect of a fracture-surface coating material. The right-hand side of (13) is multiplied by 2 to account for moisture exchange at both sides of the rock matrix adjacent to the fracture. It is clear from (9) that the driving force for the gradient $\partial \psi_m/\partial x$ is the pressure head difference between the fracture and the rock matrix.

The coefficients $C(\psi)$ and $k_r(\psi)$ are highly nonlinear functions of the pressure head potential, and consequently, the system of coupled equations (1), (2), and (13) is also highly nonlinear. Therefore, in order to solve for the pressure head field in both the fracture and the rock matrix, it is essential to define the characteristic functional relationships $k_r(\psi)$ and $C(\psi)$. In this work, the relationships derived by van Genuchten [1980] are employed, because of their applicability to many different rocks and soils [Zimmerman and Bodvarsson, 1989]. These relationships are given by

$$k_r = S_e^{1/2}[1 - (1 - S_e^{1/\eta})^\eta]^2, \qquad (14)$$

$$\theta = \theta_r + \frac{\theta_s - \theta_r}{(1 + |\alpha\psi|^\beta)^\eta}, \qquad (15)$$

$$C = \frac{d\theta}{d\psi} = -\eta(1 + |\alpha\psi|^\beta)^{-\eta-1}\beta\alpha|\alpha\psi|^{\beta-1}(\theta_s - \theta_r), \qquad (16)$$

where $S_e$ is the effective saturation ($S_e = (\theta - \theta_r)/(\theta_s - \theta_r)$); $\theta$ is the volumetric moisture content; subscripts $r$ and $s$ refer to the residual and saturated volumetric moisture content, respectively; and $\alpha$, $\beta$, and $\eta$ are empirical coefficients. The Mualam-based conductivity model is assumed to be applicable (i.e., $\eta = 1 - 1/\beta$) [van Genuchten, 1980]. It should be noted that the coefficients $\alpha$, $\beta$, $\eta$, $\theta_r$, and $\theta_s$ are all fitting parameters and that $\theta_r$ and $\theta_s$ do not possess precise definitions [van Genuchten et al., 1991]. In addition, the residual volumetric moisture content is assumed to be negligible in both the fracture and the rock matrix (see Table 1). The two coefficients $\alpha$ and $\beta$ determine the shape of the $k_r(\psi)$ and $C(\psi)$ relationships or, equivalently, the saturation/desaturation behavior. Because the fracture aperture is variable, the saturation/desaturation behavior is expected to fluctuate spatially within the fracture plane. Assuming that the values of $\alpha$ and $\beta$ are linear functions of the aperture size, the data reported by Kwicklis and Healy [1993] ($\alpha = 2.45$ m$^{-1}$, $\beta = 3.57$ for $b = 25$ $\mu$m and $\alpha = 14.58$ m$^{-1}$, $\beta = 2.92$ for $b = 125$ $\mu$m) are used to determine $k_r(\psi)$ and $C(\psi)$. The scaling of $\alpha$ linearly to $b$ is also consistent with the classical work of Leverett [1941] in which the universal J-Leverett function varies linearly with capillary suction. The coefficient $\beta$ is essentially the same as the pore size distribution index in the Brooks and Corey's relationships, which are often used to describe $k_r(\psi)$ and $C(\psi)$ in porous media [Corey, 1994]. The pore size distribution index varies with grain size distribution, structure, and mixing of the media, with the grain size distribution being the least important [Corey, 1994]. One might argue whether a pore

**Table 1.** Parameter Values for the Flow Model

| Parameter | Value | Reference |
|---|---|---|
| *Fracture* | | |
| $\alpha$ | 1.5–20.0 m$^{-1}$ | *Kwicklis and Healy* [1993] |
| $\beta$ | 2.2–3.6 | *Kwicklis and Healy* [1993] |
| $\gamma$ | $9.78 \times 10^3$ N/m$^3$ | *Munson et al.* [1994] |
| $\theta_r$ | 0.0 | |
| $\theta_s$ | 1.0 | |
| $\mu$ | $1.15 \times 10^{-8}$ N d/m$^2$ | *Munson et al.* [1994] |
| $\psi_{i_f}$ | $-10.0$ m | |
| $\psi_0$ | 0.0 m | |
| *Rock Matrix* | | |
| $K_m$ | 0.01 m/d | *Klavetter and Peters* [1986] |
| $\alpha$ | 0.15 m$^{-1}$ | *Klavetter and Peters* [1986] |
| $\beta$ | 1.5 | *Klavetter and Peters* [1986] |
| $\theta_r$ | 0.0 | |
| $\theta_s$ | 0.005 | *Abelin* [1986] |
| $\psi_{i_m}$ | $-10.0$ m | |

size distribution index exists for a segment of a fracture with constant aperture (perhaps analogous to porous media with a uniform pore size distribution). Since available experimental data indicate that the pore size distribution index for sands with uniform pore size is approximately 5 or 6 [*Wygal*, 1963; *Corey*, 1994], a value of $\beta$ for a fracture of constant aperture could exist. However, additional research is needed to confirm this and to provide accurate relationships for the variation of $\beta$ with aperture size.

Figure 3 illustrates the initial volumetric moisture content in the fracture plane, evaluated using (15) with the appropriate $\alpha$ and $\beta$ values corresponding to the realization of the aperture field presented in Figure 2. Although the initial pressure head is the same everywhere in the fracture plane (see Table 1), the volumetric moisture content varies over 4 orders of magnitude (see Figure 3). This is because the variability of the fracture aperture leads to different moisture-holding capacities. Large
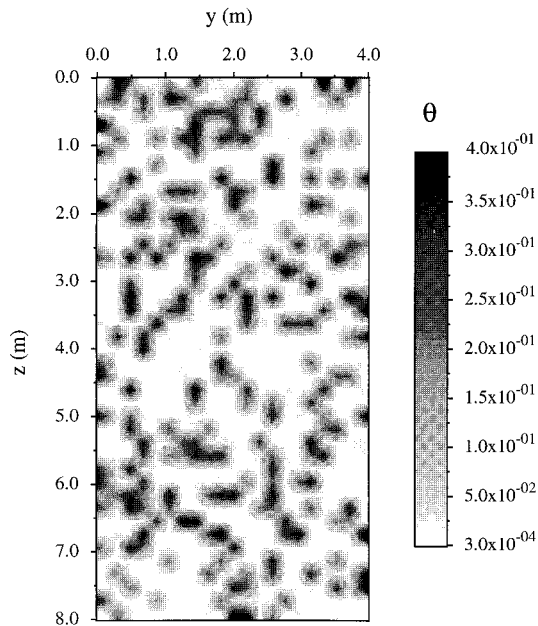
aperture areas do not hold moisture as effectively as small aperture areas, for the same pressure head. Owing to large differences in pore sizes and geometry between fractures and the rock matrix, the shape of $k_r(\psi)$ and $C(\psi)$ is expected to be quite different for the rock matrix and the fracture [*Pruess and Wang*, 1987]. For the rock matrix the values for $\alpha$ and $\beta$ used are constant, and they are listed in Table 1. Consequently, both the initial pressure head and the initial volumetric moisture content are constant throughout the rock matrix. The parameters $k_r(\psi)$ and $C(\psi)$ are considered to exhibit no hysteretic behavior, neither in the fracture nor in the rock matrix.

## Numerical Formulation

Because of the symmetry about the $z$ axis of the physical system examined (see Figure 1), only one half of the system is considered. The fracture in the $y$-$z$ plane is superimposed by a two-dimensional finite element mesh of regular size, where each node of the mesh is assigned a different aperture as generated by the geostatistical code COVAR. The rock matrix is divided into a series of two-dimensional finite element meshes of regular size. The nodes of each rock matrix mesh in the $x$-$z$ plane (i.e., perpendicular to the fracture plane) share the same location with nodes in the fracture mesh at $x = b/2$ (see Figure 4). In this work, two-dimensional three-node elements are used in the fracture plane and the rock matrix. A total of 861 nodes and 1600 elements are used in the fracture plane. The size of each element is 0.2 m in both the $y$ and $z$ directions. It should be noted that the same nodes are used for geostatistical realizations and computational flow simulations. The rock matrix is divided into 21 equally spaced meshes along the fracture width, where each mesh contains 328 nodes and 560 elements of dimensions 0.143 and 0.2 m in the $x$ and $z$ directions, respectively.

Substituting (13) into (1) and following the standard Galerkin finite element method as outlined by *Pinder and Gray* [1977] and *Huyakorn and Pinder* [1983], using Green's theorem

**Figure 3.** Initial volumetric moisture content in the fracture plane corresponding to the realization shown in Figure 2. The coded scale illustrates volumetric moisture content between $3.0 \times 10^{-4}$ and $4.7 \times 10^{-1}$.
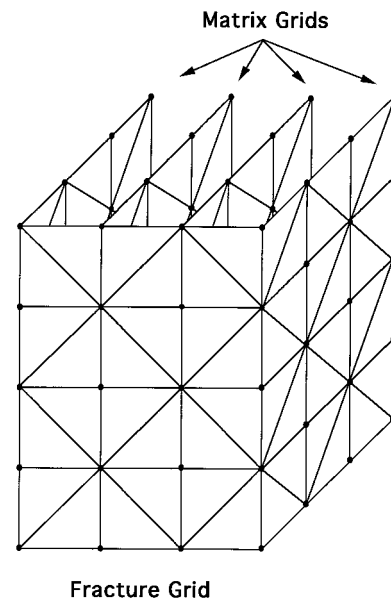
**Figure 4.** Schematic illustration of the fracture and rock matrix finite element meshes (the solid circles represent the nodes of the mesh).

to integrate the spatial derivatives, and finite differencing the time derivatives results in the following set of matrix equations

$$\mathbf{A}_f^{n+\varepsilon}[\varepsilon\boldsymbol{\Psi}_f^{n+1} + (1-\varepsilon)\boldsymbol{\Psi}_f^{n}] + \frac{\mathbf{B}_f^{n+\varepsilon}}{\Delta t}[\boldsymbol{\Psi}_f^{n+1} - \boldsymbol{\Psi}_f^{n}] = \mathbf{F}_f^{n+\varepsilon}$$

$$+ \mathbf{G}_f^{n+\varepsilon}, \qquad (17)$$

$$\mathbf{A}_m^{n+\varepsilon}[\varepsilon\boldsymbol{\Psi}_m^{n+1} + (1-\varepsilon)\boldsymbol{\Psi}_m^{n}] + \frac{\mathbf{B}_m^{n+\varepsilon}}{\Delta t}[\boldsymbol{\Psi}_m^{n+1} - \boldsymbol{\Psi}_m^{n}] = \mathbf{F}_m^{n+\varepsilon}, \qquad (18)$$

where the matrices $\mathbf{A}_f$ and $\mathbf{B}_f$ are symmetric and of the order of $N \times N$, while $\boldsymbol{\Psi}_f$, $\mathbf{F}_f$, and $\mathbf{G}_f$ are vectors of the order of $N \times 1$, where $N$ is the number of nodes in the fracture mesh; similarly, the matrices $\mathbf{A}_m$ and $\mathbf{B}_m$ are symmetric and of the order of $M \times M$, while $\boldsymbol{\Psi}_m$ and $\mathbf{F}_m$ are vectors of the order of $M \times 1$, where $M$ is the number of nodes in each mesh of the rock matrix; superscripts $n + 1$ and $n$ indicate the current and previous time levels, respectively; $\varepsilon$ is a time-weighting factor, which is set to 0.5 for unsaturated nodes and 1.0 for saturated nodes [*Huyakorn and Pinder*, 1983]; and $\Delta t$ is the incremental simulation time step. The elements of the above matrices are given as

$$A_{f_{ij}} = \frac{\gamma}{12\mu} \int\int_{D_f} b^3 k_{r_f}\left(\frac{\partial \Lambda_j}{\partial z}\frac{\partial \Lambda_i}{\partial z} + \frac{\partial \Lambda_j}{\partial y}\frac{\partial \Lambda_i}{\partial y}\right) dy\, dz, \qquad (19)$$

$$B_{f_{ij}} = \int\int_{D_f} b C_f \Lambda_i \delta_{ij}\, dy\, dz, \qquad (20)$$

$$F_{f_j} = \frac{\gamma}{12\mu} \int\int_{D_f} b^3 k_{r_f}\frac{\partial \Lambda_j}{\partial z}\, dy\, dz, \qquad (21)$$

$$G_{f_j} = 2K_m \int\int_{D_f} k_{r_m}\left(\psi_k\frac{\partial \Lambda_k}{\partial x}\right)\Lambda_j\, dy\, dz, \qquad (22)$$

$$A_{m_{kl}} = K_m \int\int_{D_m} k_{r_m}\left(\frac{\partial \Lambda_l}{\partial z}\frac{\partial \Lambda_k}{\partial z} + \frac{\partial \Lambda_l}{\partial x}\frac{\partial \Lambda_k}{\partial x}\right) dx\, dz, \qquad (23)$$

$$B_{m_{kl}} = \int\int_{D_m} C_m \Lambda_k \delta_{kl}\, dx\, dz, \qquad (24)$$

$$F_{m_l} = K_m \int\int_{D_m} k_{r_m}\frac{\partial \Lambda_l}{\partial z}\, dx\, dz, \qquad (25)$$

where $D_f$ is the spatial domain of the fracture mesh, $D_m$ is the spatial domain of a single mesh in the rock matrix (all rock matrix meshes have the same spatial domain), $\Lambda$ is a set of global piecewise linear basis functions; subscripts $i$ and $j$ vary from 1 to $N$, and subscripts $k$ and $l$ vary from 1 to $M$. The Kronecker deltas, $\delta_{ij}$ and $\delta_{kl}$, which appear in (20) and (24), respectively, are used as basis functions instead of $\Lambda$, in order to yield a mass-lumped (diagonalized) coefficient matrix for the specific moisture capacity terms. A diagonalized coefficient matrix leads to a stable numerical solution [*Milly*, 1985]. It should be noted that the integrals in (22)–(25) are repeated for each mesh of the rock matrix.

For every time step, (17) and (18) are solved iteratively using the Picard method as outlined by *Huyakorn and Pinder* [1983]. The iterative solution for the fracture is

$$\mathbf{J}_f^{n+\varepsilon,r}\Delta\boldsymbol{\Psi}_f^{n+1,r+1} = \mathbf{R}_f^{n+\varepsilon,r}, \qquad (26)$$

where

$$\mathbf{J}_f^{n+\varepsilon,r} = \varepsilon\mathbf{A}_f^{n+\varepsilon,r} + \frac{\mathbf{B}_f^{n+\varepsilon,r}}{\Delta t}, \qquad (27)$$

$$\Delta\boldsymbol{\Psi}_f^{n+1,r+1} = \boldsymbol{\Psi}_f^{n+1,r+1} - \boldsymbol{\Psi}_f^{n+1,r}, \qquad (28)$$

$$\mathbf{R}_f^{n+\varepsilon,r} = \mathbf{H}_f^{n+\varepsilon,r} - \mathbf{J}_f^{n+\varepsilon,r}\boldsymbol{\Psi}_f^{n+1,r}, \qquad (29)$$

$$\mathbf{H}_f^{n+\varepsilon,r} = \mathbf{F}_f^{n+\varepsilon,r} + \mathbf{G}_f^{n+\varepsilon,r} - \left[(1-\varepsilon)\mathbf{A}_f^{n+\varepsilon,r} - \frac{\mathbf{B}_f^{n+\varepsilon,r}}{\Delta t}\right]\boldsymbol{\Psi}_f^{n}, \qquad (30)$$

where superscripts $r$ and $r + 1$ indicate the previous and present iteration levels, respectively, at the time level $n + 1$. The solution is expressed in terms of $\Delta\boldsymbol{\Psi}$ rather than $\boldsymbol{\Psi}$ to reduce computer round off errors. Equation (26) represents a set of linear equations with as many unknowns, $\Delta\Psi^{n+1,r+1}$, as the number of nodes in the fracture plane. The Picard iterative solution for the rock matrix is derived in a similar fashion to the solution presented for the fracture. An automatic time marching algorithm is also employed, which increases or decreases the time step depending on the number of iterations needed for convergence. The initial time step is set to $7.0 \times 10^{-5}$ days and increases progressively with simulation time to a preselected maximum value of 0.05 day. Furthermore, (16) is replaced by the following relation, in order to improve the convergence of the nonlinear iterations [*Huyakorn and Thomas*, 1984],

$$C = \frac{d\theta}{d\psi} = \frac{\theta^{n+\varepsilon,r+1} - \theta^{n+\varepsilon,r}}{\psi^{n+1,r+1} - \psi^{n+1,r}}. \qquad (31)$$

However, for the case where the denominator in (31) approaches zero (i.e., impending convergence), the estimation of the specific moisture capacity is obtained by (16). All integrations (equations (19)–(25)) are performed on an element-by-element basis by using a set of local linear basis functions ($\lambda$) defined over the element and the integral equation presented by *Segerlind* [1984, equation (6.29)]. The dependent variables, $\psi_f$ and $\psi_m$, and the parameters, $b$, $C$, and $k_r$, are approximated over each element in terms of the local basis functions and their corresponding nodal values (e.g., $\psi_f \simeq \psi_{f_1}\lambda_1 + \psi_{f_2}\lambda_2 + \psi_{f_3}\lambda_3$, where the subscripts 1, 2, and 3 refer to nodes 1, 2, and 3, respectively). Since the shape functions are linear, it follows that $\psi_f$, $\psi_m$, $b$, $C$, and $k_r$ vary linearly between the nodes of each element.

## Model Testing

The numerical solution for the model presented in this work, for the case of constant fracture aperture and without moisture exchange with the rock matrix, is tested against the numerical code HYDRUS [*Kool and van Genuchten*, 1991]. HYDRUS is a one-dimensional flow and transport model for variably saturated porous media. In order to compare the fracture model to HYDRUS, the relationship $K = \gamma b^2/12\mu$ is employed to estimate the saturated hydraulic conductivity which corresponds to a desired $b$. A saturated hydraulic conductivity of 1 m/d is used in HYDRUS, which corresponds to a fracture aperture of 3.8 $\mu$m. Furthermore, equivalent boundary conditions to (4) and (5) were used in HYDRUS (i.e., constant
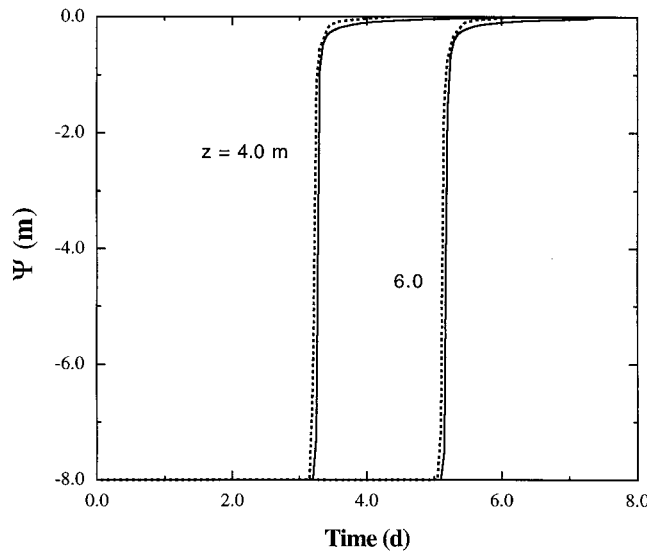
**Figure 5.** Comparison between temporal distributions of the pressure head potential created by the presented numerical solution (dotted lines) and the one-dimensional numeric code HYDRUS (solid lines) for two different depths (here $b = 3.8$ $\mu$m, $K = 1.0$ m/d, $\alpha = 2.0$ m$^{-1}$, $\beta = 3.0$, and $\psi_0 = 0.05$ m).



**Figure 6.** Spatial distribution of the pressure head potential in the fracture plane for unsaturated flow without moisture exchange with the rock matrix (here $t = 1$ day).

pressure head top boundary, $\psi = \psi_0$, and free draining bottom boundary, $\partial \psi / \partial z = 0$). Figure 5 shows a comparison between the present numerical solution and HYDRUS at $z$ equal to 4 and 6 m. The two solutions are in very good agreement. It should be noted that Figure 5 also illustrates the sharp interface of the moisture front which is a common characteristic of unsaturated flow in homogeneous porous media and fractures with constant apertures.

## Model Simulations and Discussion

In order to investigate the effect of variable aperture and moisture exchange with the rock matrix on unsaturated flow in the fracture considered, several model simulations under different physical conditions have been performed. The parameter values used in the simulations are compiled in Table 1. First, we examined the case where there is no moisture exchange with the rock matrix (i.e., $\Omega = 0$). Figure 6 portrays a two-dimensional snapshot of the pressure head potential in the fracture plane after 1 day of simulation time. The area adjacent to the top boundary is almost saturated, and there is no significant fingering. This is due to the high gradient imposed by the constant pressure head at the top boundary, which leads to saturation of areas with smaller aperture followed by saturation of areas with progressively larger apertures. Further away from the top boundary, more variability in the pressure head and more pronounced fingering is observed, because of the fluctuations in the moisture holding capacity of areas with different aperture sizes. At low pressure head potentials, areas with large apertures do not hold as much moisture as areas with small apertures (see (15)). Therefore areas with small aperture dominate the flow causing localized pressure buildup and possible reversal of pressure head potential gradients. Pressure buildup in small aperture areas does not only depend on aperture size but also on the spatial location of other neighboring areas with comparatively the same aperture size. An area of very small aperture size completely surrounded by
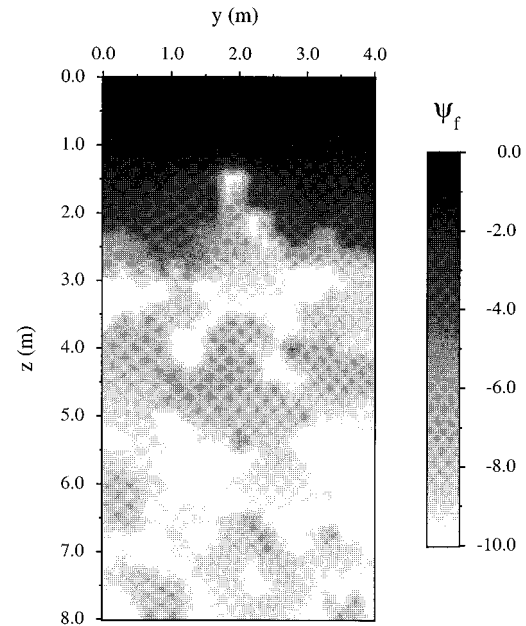
areas of large aperture size could remain at a low pressure head potential for a long time.

It should be noted that the snapshot shown in Figure 6 corresponds to a single realization of the aperture field. However, the results of unsaturated flow in a variable aperture fracture are best illustrated by the ensemble average of several aperture realizations (i.e., expected value). Figure 7 displays curves for pressure distribution as a function of time, based on an ensemble average of 25 realizations for the case where $\Omega = 0$. The pressure head potential is averaged across the fracture
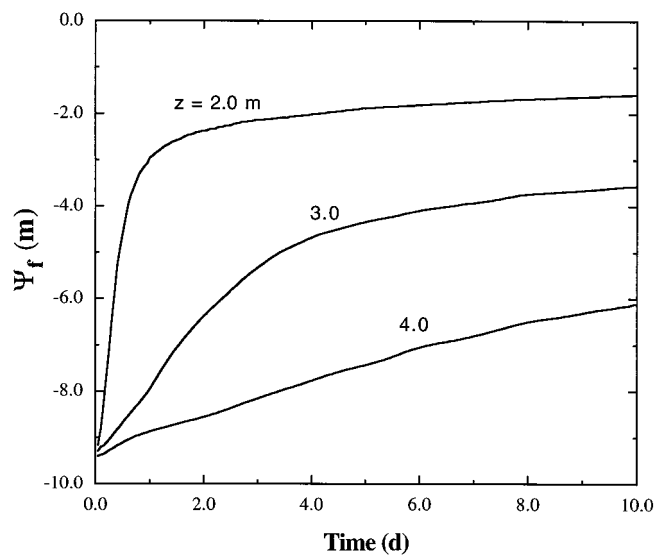


**Figure 7.** Temporal distribution of the ensemble mean pressure head potential averaged across the fracture width at 2.0, 3.0, and 4.0 m downstream from the top boundary, for unsaturated flow without moisture exchange with the rock matrix (here $\Omega = 0$).

width at 2, 3, and 4 m from the top boundary. The number of realizations is chosen such that additional realizations do not change the calculated ensemble average. These curves indicate that the fracture aperture variability leads to a slower increase in the pressure head with time (the fronts are not as sharp as the ones observed in Figure 5) and that the rate of pressure buildup decreases with distance from the top boundary. This is because fracture segments with small aperture fill with moisture faster than areas with large aperture. Furthermore, the gradual pressure increase is due to the time period required for areas with large aperture to fill with moisture.

The impact of the standard deviation ($\sigma$) of the lognormally distributed fracture aperture fluctuations on the ensemble average pressure head potential, for the case of flow without moisture exchange with the rock matrix is shown in Figure 8. The pressure head potential curves are based on 25 realizations of the fracture aperture fluctuations at a distance of 2 and 3 m from the top boundary. The number of realizations is chosen such that additional realizations do not change the calculated ensemble average. The solid lines correspond to $\sigma$ = 0.43 $\mu$m, and the dotted lines correspond to $\sigma$ = 0.3 $\mu$m. These values of the standard deviation are for the log of the aperture. It is clear from Figure 8 that decreasing the standard deviation leads to a decrease in the moisture flow in the fracture. In addition, the difference between the simulated pressure head potentials for the two standard deviations examined increases with distance downstream of the top boundary. This is because increasing the standard deviation leads to a greater variability in the aperture distribution within the fracture plane, which in turn increases the number of areas with smaller aperture. The greater the number of areas with small apertures present in the fracture, the faster the moisture movement and pressure buildup.

Figure 9 shows simulated breakthrough curves for an ensemble average of 25 realizations for different correlation lengths (0.3 and 0.5) at distances 2 and 3 m downstream from the inlet boundary. The pressure head potential is lower for the larger correlation length (0.5). This is because increasing the
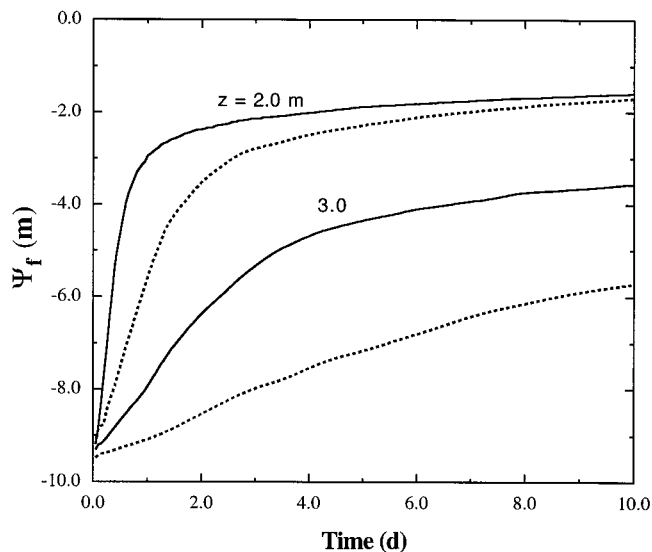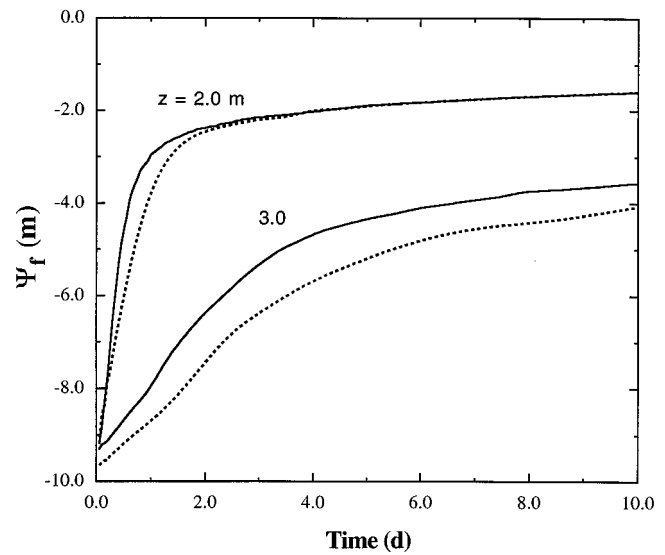


**Figure 9.** Temporal distribution of the ensemble mean pressure head potential averaged across the fracture width at 2.0 and 3.0 m downstream from the top boundary, for correlation lengths 0.3 (solid lines) and 0.5 (dotted lines) (here $\Omega = 0$).

correlation length leads to enhanced preferential moisture flow. Small aperture areas are most likely surrounded by small aperture areas, and large aperture areas are surrounded by large aperture areas. Consequently, for large correlation lengths it is expected that moisture is transported through fewer channels across the fracture width. The breakthrough curves presented are obtained by averaging the pressure head potential across the entire fracture width; therefore the pressure head potential is lower for the larger correlation length.

The effect of moisture exchange with the rock matrix (i.e., $\Omega \neq 0$) on unsaturated flow in the fracture is illustrated in Figure 10. The initial pressure head potential in the rock matrix is assumed to be uniform and equal to that in the fracture, $\psi_{i_m} = \psi_{i_f}$ (see Table 1). Figure 10 shows a two-dimensional snapshot of the pressure head potential in the fracture plane after 1 day of simulation time. It is clear that the fingering and pressure variation across the fracture width are considerably decreased by comparison to the case where there is no moisture exchange with the rock matrix (Figure 6). This is because the rock matrix acts as a sink that absorbs moisture from the fracture, which in turn smoothes the effect of the fracture aperture variability.

The pressure head potential in the fracture for the case where there is moisture exchange with the rock matrix is obtained by accounting for $\Omega$ in the model. Figure 11 shows a comparison between the cases with and without moisture exchange with the rock matrix for an ensemble average of 25 realizations at a distance of 2 and 3 m from the top boundary. The solid lines represent the case of no moisture exchange with the rock matrix, and the dotted lines represent the case of moisture exchange with the rock matrix. It is evident from Figure 11 that moisture exchange with the rock matrix decreases the pressure head potentials in the fracture. Also, the effect of moisture exchange becomes more pronounced with increasing distance downstream from the top boundary. This is because areas close to the constant pressure head top boundary are replenished at a faster rate. Farther downstream, the moisture removed by the rock matrix originates predominantly
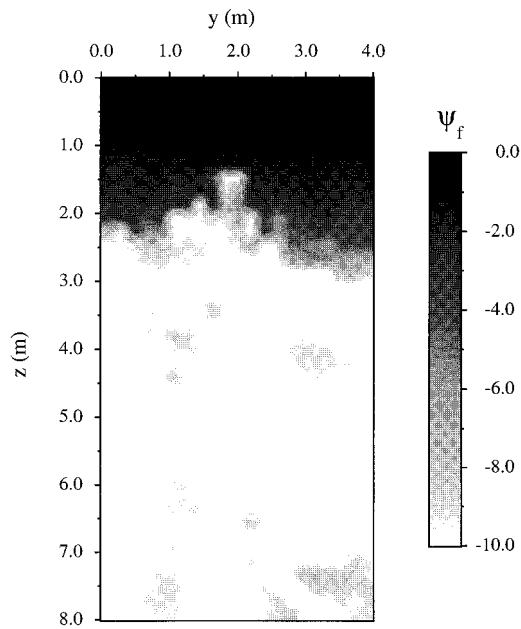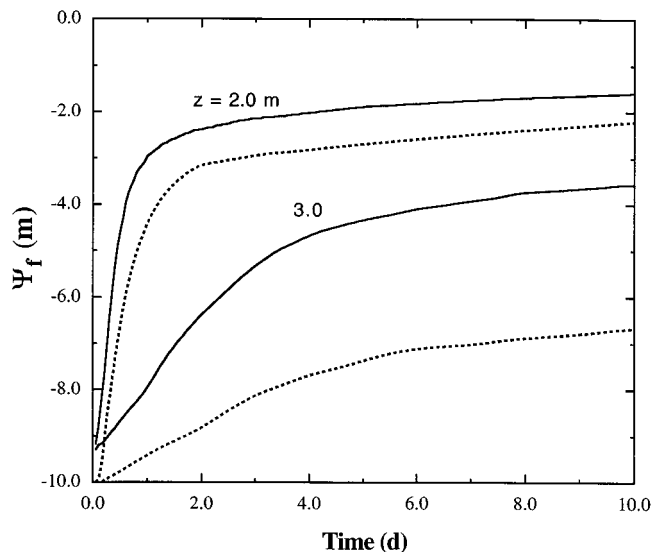


**Figure 8.** Temporal distribution of the ensemble mean pressure head potential averaged across the fracture width at 2.0 and 3.0 m downstream from the top boundary, for $\sigma$ = 0.43 (solid lines) and $\sigma$ = 0.3 (dotted lines) (here $\Omega = 0$).

**Figure 10.**  Spatial distribution of the pressure head potential in the fracture plane for unsaturated flow with moisture exchange with the rock matrix (here $t = 1$ day).

from fracture areas with small aperture. This reduction in moisture from fracture areas with small aperture further hinders fracture segments with large aperture from filling with moisture. Furthermore, Figure 11 indicates that the curves corresponding to cases of with and without moisture exchange with the rock matrix at distance 2 m slowly approach each other, whereas in Figure 8 the curves corresponding to standard deviations 0.43 and 0.3 $\mu$m approach each other at a faster rate. This is because moisture exchange with the rock matrix leads to moisture absorption by the fracture.

The effect of fracture-surface coatings on unsaturated flow in the fracture is shown in Figure 12. The simulated breakthrough curves are for the ensemble average of 25 realizations for different fracture-surface effective hydraulic conductivities. The uppermost curve corresponds to the case where there is no fluid interaction with the rock matrix (i.e., $\Omega = 0$). The lowermost curve corresponds to the case where the fracture surface is free of any coating material (i.e., $K_e = K_m$). It is clear from Figure 12 that as the fracture-surface effective hydraulic conductivity decreases, which indicates the existence of a mineralized layer or coating on the fracture surface, the pressure head potential in the fracture increases. This is because fracture-surface coatings inhibit moisture absorption by the rock matrix, resulting in a fluid flow primarily within the fracture.

## Summary and Conclusions

Previous work on flow in unsaturated fractured media usually accounted for moisture exchange between the fracture and the rock matrix or fracture aperture variability but not both. In this study, unsaturated flow in a quasi-three-dimensional fracture-rock matrix system with spatially variable aperture accounting for moisture exchange with the rock matrix is investigated. The fracture aperture is treated as a stochastic variable, whereas the rock matrix is assumed to be homogeneous and isotropic. The resulting set of coupled nonlinear equations, with the pressure head as the dependent variable, is solved numerically using the finite element method with two-dimensional triangular elements and linear basis functions. The equations are linearized using the Picard iterative scheme with an automatic time step.

Spatial and temporal distributions of the pressure head potential in a fracture are constructed for various situations. The results indicate that the variability in the fracture aperture causes fingering in the pressure head distribution within the fracture plane. Moisture exchange with the rock matrix is found to remove moisture from the fracture thereby decreas-
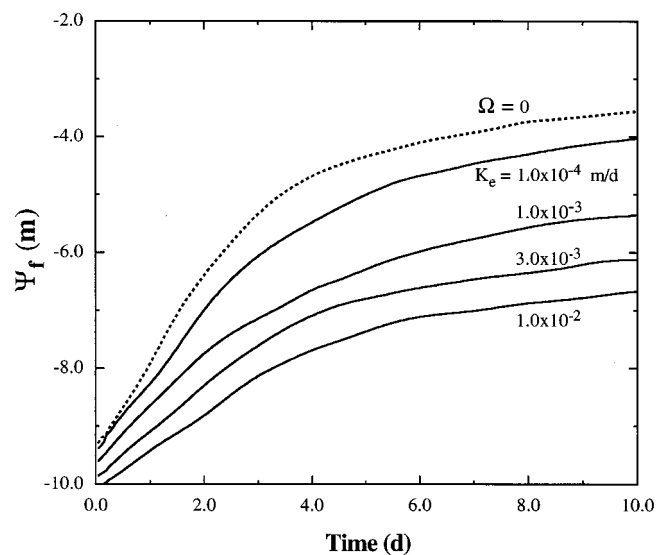


**Figure 11.**  Temporal distribution of the ensemble mean pressure head potential averaged across the fracture width at 2.0 and 3.0 m downstream from the top boundary, for unsaturated flow with moisture exchange with the rock matrix (dotted lines) and without moisture exchange with the rock matrix (solid lines).



**Figure 12.**  Temporal distribution of the ensemble mean pressure head potential averaged across the fracture width at 3.0 m downstream from the top boundary for several fracture-surface effective hydraulic conductivities. Top curve represents the case where $\Omega = 0$.

ing the effects of aperture variability and diminishing the fingering of the pressure head distribution in the fracture plane. Furthermore, fracture-surface coatings decrease the effect of the rock matrix in slowing down the moisture movement. In addition, an increase in the standard deviation of the lognormally distributed fracture aperture leads to a faster increase in the pressure head potential with time, whereas large correlation lengths lead to a decrease in the amount of moisture flowing across the fracture width.

## Notation

$b$   fracture aperture, $L$.

$C$   specific moisture capacity, $1/L$.

$k_r$   relative permeability.

$K$   saturated hydraulic conductivity, $L/t$.

$K_e$   fracture-surface effective hydraulic conductivity, $L/t$.

$l_x$   representative depth of the rock matrix in the $x$ direction, $L$

$l_y$   fracture width in the $y$ direction, $L$

$l_z$   fracture-rock matrix length in the $z$ direction, $L$

$M$   number of nodes in each mesh of the rock matrix.

$N$   number of nodes in the fracture mesh.

$S_e$   effective saturation, equal to $(\theta - \theta_r)/(\theta_s - \theta_r)$.

$t$   time, $t$.

$x$   horizontal coordinate perpendicular to the fracture plane, $L$.

$y$   horizontal coordinate along the fracture width, $L$.

$z$   vertical coordinate along the fracture length, $L$.

### Greek Letters

$\alpha$   empirical coefficient.

$\beta$   empirical coefficient.

$\gamma$   fluid specific weight, $M/L^2t^2$.

$\Delta t$   incremental simulation time step, $t$.

$\varepsilon$   time-weighting factor.

$\eta$   empirical coefficient, equal to $1 - 1/\beta$.

$\theta$   volumetric moisture content.

$\lambda$   local linear basis function.

$\Lambda$   global linear basis function.

$\mu$   fluid dynamic viscosity, $M/Lt$.

$\sigma$   standard deviation of the lognormally distributed fluctuations of the fracture aperture

$\psi$   pressure head potential, $L$.

$\Omega$   fracture-rock matrix cross-flow term, $L/t$.

### Subscripts

$f$   fracture.

$i,j$   indices for the nodes in the fracture mesh.

$k,l$   indices for the nodes in each mesh of the rock matrix.

$m$   rock matrix.

$r$   residual volumetric moisture content.

$s$   saturated volumetric moisture content.

### Superscripts

$n$   time level.

$r$   iteration level.

## References

Abdel-Salam, A., Modeling of contaminant/colloid transport and unsaturated flow in fractured media, Ph.D. dissertation, 195 pp., Dep. of Civ. and Environ. Eng., Univ. of Calif., Irvine, 1995.

Abdel-Salam, A., and C. V. Chrysikopoulos, Modeling of colloid and colloid-facilitated contaminant transport in a two-dimensional fracture with spatially variable aperture, *Transp. Porous Media*, *20*(3), 197–221, 1995.

Abelin, H., Migration in a single fracture: An in situ experiment in a natural fracture, Ph.D. dissertation, 170 pp., Dep. of Chem. Eng., R. Inst. of Tech., Stockholm, 1986.

Bourke, P. J., Channeling of flow through fractures in rock, paper presented at GEOVAL87 Symposium, Swed. Nucl. Power Inst., Stockholm, 1987.

Carlos, B. A., Minerals in fractures of the unsaturated zone from drill core USW G-4, Yucca Mountain, Nye County, Nevada, *Rep. LA-10415-MS*, Los Alamos Natl. Lab., Los Alamos, N. M., 1985.

Corey, A. T., *Mechanics of Immiscible Fluids in Porous Media*, rev. ed., 252 pp., Water Resour. Pub., Fort Collins, Colo. 1994.

Dykhuizen, R. C., Transport of solutes through unsaturated fractured media, *Water Res.*, *21*(12), 1531–1539, 1987.

Evans, D. D., and T. J. Nicholson, Flow and transport through unsaturated fractured rock: An overview, in *Flow and Transport Through Unsaturated Fractured Rock*, *Geophys. Monogr. Ser.*, vol. 42, edited by D. D. Evans and T. J. Nicholson, pp. 1–10, AGU, Washington, D. C., 1987.

Gerke, H. H., and M. T. van Genuchten, A dual-porosity model for simulating the preferential movement of water and solutes in structured porous media, *Water Resour. Res.*, *29*(2), 305–319, 1993.

Huyakorn, P. S., and G. F. Pinder, *Computational Methods in Subsurface Flow*, 473 pp., Academic, San Diego, Calif., 1983.

Huyakorn, P. S., and S. D. Thomas, Techniques for making finite elements competitive in modeling flow in variably saturated porous media, *Water Resour. Res.*, *20*(8), 1099–1115, 1984.

Klavetter, E. A., and R. R. Peters, Estimation of hydrologic properties for an unsaturated fractured rock mass, *Rep. SAND 84-2642*, Sandia Natl. Lab., Albuquerque, N. M., 1986.

Kool, J. B., and M. T. van Genuchten, HYDRUS one-dimensional variably saturated flow and transport model, including hysteresis and root water uptake, report, 101 pp., U.S. Salinity Lab., U.S. Dep. of Agric., Riverside, Calif., 1991.

Kwicklis, E. D., and R. W. Healy, Numerical investigation of steady liquid water flow in a variably saturated fracture network, *Water Resour. Res.*, *29*(12), 4091–4102, 1993.

Leverett, M. C., Capillary behavior in porous media, *Trans. Am. Inst. Min. Metall. Pet. Eng.*, *142*, 341–358, 1941.

Martinez, M. J., R. C. Dykhuizen, and R. R. Eaton, The apparent conductivity for steady unsaturated flow in periodically fractured porous media, *Water Resour. Res.*, *28*(11), 2879–2887, 1992.

Milly, P. C. D., A mass-conservative procedure for time-stepping in models of unsaturated flow, *Adv. Water Resour.*, *8*, 32–36, 1985.

Munson, B. R., D. F. Young, and T. H. Okiishi, *Fundamentals of Fluid Mechanics*, 893 pp., John Wiley, New York, 1994.

Neretnieks, I., Transport in fractured rocks, *Mem. Int. Assoc. Hydrogeol.*, *17*, 301–318, 1985.

Nitao, J. J., and T. A. Buscheck, Infiltration of a liquid front in an unsaturated fractured porous medium, *Water Resour. Res.*, *27*(8), 2099–2112, 1991.

Pinder, G. F., and W. G. Gray, *Finite Element Simulation in Surface and Subsurface Hydrology*, 295 pp., Academic, San Diego, Calif., 1977.

Pruess, K., and Y. W. Tsang, On two-phase relative permeability and capillary pressure of rough-walled rock fractures, *Water Resour. Res.*, *26*(9), 1915–1926, 1990.

Pruess, K., and J. S. Y. Wang, Numerical modeling of isothermal and nonisothermal flow in unsaturated fractured rock: A review, in *Flow and Transport Through Unsaturated Fractured Rock*, *Geophys. Monogr. Ser.*, vol. 42, edited by D. D. Evans and T. J. Nicholson, pp. 11–21, AGU, Washington, D. C., 1987.

Segerlind, L. J., *Applied Finite Element Analysis*, 427 pp., John Wiley, New York, 1984.

Thoma, S. G., D. P. Gallegos, and D. M. Smith, Impact of fracture coatings on fracture/matrix flow interactions in unsaturated, porous media, *Water Resour. Res.*, *28*(5), 1357–1367, 1992.

U.S. Department of Energy, Final environmental assessment-Yucca Mountain site, Nevada Research and Development Area, Nevada,

*Rep. DOE/RW-0012*, Off. Civil. Radioactive Waste Manage., Washington, D. C., 1986.

van Genuchten, M. T., A closed form equation for predicting the hydraulic conductivity of unsaturated soils, *Soil Sci. Soc. Am. J.*, *44*(5), 892–898, 1980.

van Genuchten, M. T., F. J. Leij, and S. R. Yates, The RETC code for quantifying the hydraulic functions of unsaturated soils, *Rep. EPA/600/2-91/065*, 85 pp., Robert S. Kerr Environ. Res. Lab., Environ. Prot. Agency, Ada, Okla., 1991.

Williams, S. A., and A. I. El-Kadi, COVAR: A computer program for generating two-dimensional fields of autocorrelated parameters by matrix decomposition, *Rep. IGWMC FOS 29*, Int. Groundwater Model. Cent., Holcomb Res. Inst., Colo. Sch. of Mines, Golden, 1986.

Wilson, M. L., and A. L. Dudley, Radionuclide transport in an unsaturated fractured medium, in *Flow and Transport Through Unsatur-* *ated Fractured Rock, Geophys. Monogr. Ser.*, vol. 42, edited by D. D. Evans and T. J. Nicholson, pp. 23–29, AGU, Washington, D. C., 1987.

Wygal, R. J., Construction of models that simulate oil reservoirs, *Soc. Pet. Eng. J.*, *228*(12), 281–286, 1963.

Zimmerman, R. W., and G. S. Bodvarsson, An approximate solution for one-dimensional absorption in unsaturated porous media, *Water Resour. Res.*, *25*(6), 1422–1428, 1989.

A. Abdel-Salam and C. V. Chrysikopoulos, Department of Civil and Environmental Engineering, University of California, Irvine, Irvine, CA 92717. (e-mail: costas@eng.uci.edu)